Systematic Design of Optimal Low-Thrust Transfers for the Three-Body Problem

Shankar Kulumani · Taeyoung Lee

Abstract We develop a computational approach for the design of continuous low thrust transfers in the planar circular restricted three-body problem. The use of low thrust propulsion allows the spacecraft to depart from the natural dynamics and enables a wider range of transfers. We generate the reachable set of the spacecraft and use this to determine transfer opportunities, analogous to the intersection of control-free invariant manifolds. The reachable set is developed on a lower dimensional Poincaré section and used to design transfer trajectories. This is solved numerically as a discrete optimal control problem using a variational integrator, which preserve the geometric structure of the motion in the three-body problem. We demonstrate our approach with two numerical simulations of transfers in the Earth-Moon three-body system.

1 Introduction

Designing spacecraft trajectories is a classic and ongoing topic of research. There has been significant research into the design of orbital transfers for space vehicles. Optimal expenditure of onboard propellant is critical to allowing a mission to continue for a longer period of time or to enable the launch of a less massive spacecraft. Electric propulsion systems offer a much greater specific impulse than chemical systems and are able to operate for extended periods of time. However, these electric propulsion systems typically have much less thrust than their chemical counterparts and therefore must operate over longer durations in order to impart the

S. Kulumani · T. Lee
Department of Mechanical & Aerospace Engineering,
George Washington University,
800 22nd St NW, Washington, DC 20052.
E-mail: skulumani@gwu.edu
E-mail: tylee@gwu.edu

desired momentum change. Recent developments in miniature electric propulsion offer the potential for new research opportunities for small spacecraft [9]. With reduced development intervals and decreased launch costs, small satellites have gained increased attention as a cost effective means of scientific and technologic development. The merger of small satellites with miniature electric propulsion enables inexpensive and responsive missions requiring large changes in orbital energy or extended mission lifespan. With the potential for more demanding missions, even greater importance is placed on the mission design to ensure that optimal trajectories satisfy mission requirements. In addition, non-Keplerian orbits and multi-body dynamics have been shown to allow for a much greater range of potential missions at a reduced energy cost [15]. Future space missions are increasing in complexity and will require new classes of orbits that are not possible via the traditional patched-conic approach [25,5]. Optimally combining the dynamical structure of the three-body problem with low-thrust propulsion systems is vital for future mission success.

There has been extensive research focused on the optimal control of spacecraft orbital transfers in the three-body problem [23,6]. Typically, the optimal control problem is solved via direct methods, which approximate the continuous problem as a parameter optimization problem. The state and/or control trajectories are parameterized and solved in the form of a nonlinear optimization problem. The work in [23,6] use this direct approach in designing low-thrust transfers in the three-body problem. Alternatively, indirect methods apply calculus of variations to derive the necessary conditions for optimality. This yields a lower dimensioned problem than the direct approach and algebraic conditions that, when satisfied, guarantee local optimality in contrast to direct methods which result in sub-optimal solutions.

The application of optimal control methods for orbital trajectory design is nontrivial. In order to implement any optimization method a sufficiently accurate "initial guess" is required. Frequently, insight into the problem or intuition on the part of the designer is often required to determine initial conditions that will converge to the optimal solution. However, the three-body system dynamics are nonlinear and exhibit chaotic behaviors. Popularly refered to as the "butterfly effect" small changes in initial conditions result in large variations of the resulting system trajectory. This makes solving the optimization problem highly dependent on the initial condition. In addition, there is no closed form analytical solution for the three-body problem [27]. Since there is an insufficient number of analytical constants, or integral of motion, numerical methods must be used to investigate solutions to the three-body problem. As a result, accurate numerical methods are required to determine optimal solutions. These methods are critically dependent on accurate initial guess in order to allow for convergence to an optimal solution.

Efficient numerical implementation is dependent on correct initial conditions as well as accurate numerical integration. [23,6] implement the solutions using conventional Runge-Kutta integration techniques. These techniques suffer from numerical instability and energy drift behaviors which make them ill-suited for long-term propagation. These dissipative effects are even more detrimental with the addition of low-thrust propulsion to the dynamic equations of motion. Conventional integration techniques fail to capture the physical laws and geometric properties of the dynamic system [8]. As a result, the long term effects of low-thrust on the spacecraft trajectory are not accurately captured.

[15, 25] have illustrated the rich structure that exists in the three-body problem. Within the three-body problem, a spacecraft's feasible region of motion is constrained by its energy, or Jacobi integral. It has been shown that there exist multi-dimensional tubes, or invariant manifolds, of constant energy trajectories that span the state space. Associated with periodic solutions of the three-body dynamics, these invariant manifolds allow for the spacecraft to traverse vast expanses of the state space with zero energy change. However, the results presented are highly case specific and difficult to generalize to arbitrary transfers. Also, these results are based on control-free trajectories which rely on the underlying structure of the three-body system. In addition, transfer orbits along an invariant manifold require a longer time of flight which may be undesirable for time critical missions. The addition of low-thrust propulsion offers the potential of reduced transit times and the ability to depart from the free motion trajectory to allow for increased transfer opportunities.

In this paper, we propose a systematic design method which enables low-thrust transfers in the planar circular restricted three-body problem. Our approach avoids the difficulties in selecting an appropriate initial guess for optimization. Instead, we utilize the concept of the reachability set to enable a simple methodology of selecting initial conditions to achieve general orbital transfers. In addition, through the use of geometric integrators we accurately capture the effects of low thrust on the system dynamics in the numerical simulation. This approach avoids the instability and dissipative effects of conventional integration schemes. With this proposed method, the previous research on control-free trajectories will be generalized with the addition of low thrust propulsion systems.

To achieve these objectives, an optimal control problem is formulated to determine the reachability set on a Poincaré section. Given an initial condition and fixed time horizon, the reachable set is the set of states attainable, subject to the operational constraints of the spacecraft. Generation of this reachability set allows for the extension of the previous methods based on invariant manifolds in the three-body problem. In addition, the generation of the reachable set allows for a more systematic method of determining initial conditions and eases the burden on the designer. The Poincaré section reduces the dimensionality of the system dyanmics to the study of a related discrete update map. This allows for the study of the complex dynamics of the three-body problem on a lower dimensional space. Rather than relying on intuition or insight into the problem, states are chosen which minimize the distance towards the target on an appropriate Poincaré section. This simple methodology allows for extended transfer trajectories which iteratively approach a target region. We utilize the low thrust control input to enlarge the reachability set. Maximization of the reachability set, on an appropriately chosen Poincaré section, allows for a greater space of potential transfer trajectories. The use of the Poincaré section allows for design on a lower dimensional space and simplifies the design process.

In order to address the issues associated with conventional numerical integration, we apply computational geometric optimal control techniques. We generalize the previous work of determining orbital transfers using invariant manifolds [15]. We incorporate the effects of continuous low thrust propulsion to enable departure from the system dynamics and enable increased transfer opportunities. The dynamics of the three-body system are derived from the discrete Lagrangian, which approximates the integral of the continuous time Lagrangian over a fixed discrete step. Application

of the discrete Euler-Lagrange equations, or equivalently the discrete Legendre transform, results in the discrete equations of motion. This discrete update map, or variational integrator, shares the same geometric properties of the continuous time system and exhibits much better energy behavior than the traditional integration methods, especially over long transfer durations with small magnitude control inputs. A discrete optimal control problem is formulated from the discrete equations of motion. This approach, where explicit discretization occurs prior to optimization, is in contrast to the typical method, where the equations of motion are implicitly discretized during the optimization procedure. Formulating the problem in this manner results in more stable and accurate optimal solutions. In indirect methods the optimal control problem is expressed as a two-point boundary value problem. Optimal solutions are generally sensitive to small variations in the initial multipliers. As a result, the numerical stability of sensitivity derivatives is critical to accuracy and computational performance. The use of geometric integrators, which do not suffer the numerical dissipation of conventional integration methods, results in a more robust and efficient solution.

In short, the authors present a systematic method of generating optimal transfer orbits in the three-body problem. Previous results in the design of optimal transfers have relied on suboptimal direct optimization methods and conventional integration techniques. This paper provides a discrete optimal control formulation to generate the reachability set on a Poincaré section. We derive and solve the Euler-Lagrange equations to generate the necessary conditions for an optimal solution. This results in an optimal solution rather than the suboptimal solution typical of direct optimal control methods. In addition, the use of a geometric integrators ensures numerical stability for long-duration orbit transfers and maintains this behavior with the addition of small magnitude control inputs. Our computation of the reachable set allows for a simple metric of defining optimal trajectories. We avoid the issues inherent in selecting a valid initial condition for optimization. Rather, we choose a state on the reachability set which minimizes the distance toward the desired target. We demonstrate these capabilities via two numerical examples simulating transfer trajectories in the Earth-Moon system.

2 Planar Circular Restricted Three Body Problem

The system model is based on the planar circular restricted three body problem (PCRTBP). The Earth is assumed to be the more massive primary, m_1, while the Moon is the second, smaller primary m_2. The equations of motion are developed in a rotating reference frame which allows for much greater insight into the structure of the dynamics. The $\hat{e}_1$ axis is directed along the vector from the Earth to the Moon. The $\hat{e}_2$ axis lies in the orbital plane and is orthogonal to $\hat{e}_1$. The rotating reference frame is centered at the system barycenter. It is assumed that the $(\hat{e}_1, \hat{e}_2)$ frame rotates with a constant angular velocity equal to the mean motion of the Moon. Following convention, the system is also non-dimensionalized by the characteristic units of length, mass, and time [15]. As a result, the system can be characterized by a single mass ratio parameter μ,

$$\mu = \frac{m_2}{m_1 + m_2} \, . \tag{1}$$

The larger primary, m_1, is located at $(-\mu, 0)$ and the smaller m_2 is located at $(1 - \mu, 0)$, while the spacecraft is located at (x, y). In the rotating reference frame the Lagrangian is given by

$$L = \frac{1}{2} \left((\dot{x} - y)^2 + (\dot{y} + x)^2 \right) + \frac{1 - \mu}{r_1} + \frac{\mu}{r_2} , \tag{2}$$

where the distance $r_1, r_2 \in \mathbb{R}$ of the spacecraft to each primary is as

$$r_1 = \sqrt{(x + \mu)^2 + y^2} , \tag{3}$$

$$r_2 = \sqrt{(x - 1 + \mu)^2 + y^2} . \tag{4}$$

Application of the Euler-Lagrange equations results in following equations of motion defined in the rotating reference frame

$$\ddot{x} - 2\dot{y} + \frac{\partial U}{\partial x} = u_x ,$$

$$\ddot{y} + 2\dot{y} + \frac{\partial U}{\partial y} = u_y , \tag{5}$$

where the effective potential U is defined as

$$U = \frac{1}{2} \left(x^2 + y^2 \right) + \frac{1 - \mu}{r_1} + \frac{\mu}{r_2} , \tag{6}$$

and the control inputs is defined as $\boldsymbol{u} = \begin{bmatrix} u_x & u_y \end{bmatrix}^T \in \mathbb{R}^{2 \times 1}$. The state is defined as $\boldsymbol{x} = \begin{bmatrix} \boldsymbol{r} & \boldsymbol{v} \end{bmatrix}^T$ with $\boldsymbol{r} = \begin{bmatrix} x & y \end{bmatrix}^T \in \mathbb{R}^{2 \times 1}$ and $\boldsymbol{v} = \begin{bmatrix} \dot{x} & \dot{y} \end{bmatrix}^T \in \mathbb{R}^{2 \times 1}$ representing the position and velocity with respect to the system barycenter, respectively. The equations of motion may be rewritten in state space form as

$$\begin{bmatrix} \dot{\boldsymbol{r}} \\ \dot{\boldsymbol{v}} \end{bmatrix} = \begin{bmatrix} \boldsymbol{v} \\ A\boldsymbol{v} + \nabla U + \boldsymbol{u} \end{bmatrix} = f(t, \boldsymbol{x}, \boldsymbol{u}) , \tag{7}$$

where the matrix A and psuedo gravitational potential gradient ∇U are

$$A = \begin{bmatrix} 0 & 2 & 0 \\ -2 & 0 & 0 \\ 0 & 0 & 0 \end{bmatrix} , \tag{8}$$

$$\nabla U = \begin{bmatrix} x - \frac{(1-\mu)(x+\mu)}{r_1^3} - \frac{\mu(x-1+\mu)}{r_2^3} \\ y - \frac{(1-\mu)y}{r_1^3} - \frac{\mu y}{r_2^3} \\ -\frac{(1-\mu)z}{r_1^3} - \frac{\mu z}{r_2^3} \end{bmatrix} = \begin{bmatrix} U_x \\ U_y \\ U_z \end{bmatrix} . \tag{9}$$

2.1 Jacobi Integral

There exists a single integral, or constant of motion for the three-body problem [27, 16]. This energy constant is analogous to the total mechanical energy, however it is a non-physical quantity arising from the problem formulation [27]. Also known as the Jacobi constant, it is defined as a function of the position and velocity in the rotating frame and given by

$$E\left(\boldsymbol{r}, \boldsymbol{v}\right) = \frac{1}{2}\left(\dot{x}^2 + \dot{y}^2\right) - U\left(x, y\right) . \tag{10}$$

Equation (10) divides the phase space into distinct regions of allowable motion based on the energy level of the spacecraft. Fixing the Jacobi integral to a constant defines zero velocity curves, which are the locus of points where the kinetic energy, and hence velocity vanishes. As seen in Figure 1, the phase space is divided into distinct realms based on the energy level. In the vicinity of m_1 or m_2 there exists a potential well. As the energy level increases there are five critical points of the effective potential Eq. (6) where the slope is zero. Three collinear saddle points on the $\hat{e}_1$ axis and two equilateral points. These equilibrium, or Lagrange points, are labeled $L_i, i = 1, \dots, 5$ and are shown in Figure 1. The Jacobi integral is a valuable invariant property of the three-body system that allows for greater insight into the motion of the spacecraft.
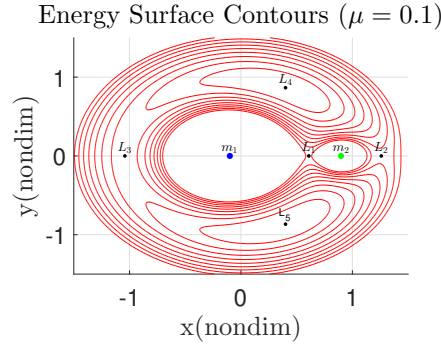

Fig. 1: Contour plot of Jacobi integral

3 Variational Integrator

Geometric numerical integration deals with numerical integration methods which preserve the geometric properties of the flow of a differential equation, such as invaraint properties and symplecticity. Variational integrators are constructed by discretizing Hamilton's principle rather than the continuous Euler-Lagrange equations [21]. As a result, integrators developed in this manner have the desirable properties that they are symplectic and momentum preserving. In addition, they exhibit improved energy behavior over long integration periods. We present a short

background on the variational principle for mechanical systems. We then develop a discrete approximation of the action integral and construct a variational integrator for the PCRTBP.

3.1 Variational Principle

Consider a continuous mechanical system described by the Lagrangian, $L(q, \dot{q})$, for the generalized position, q, and velocity, $\dot{q}$. In the standard approach of variational mechanics the action integral is formed by integrating the continuous Lagrangian along a path $q(t)$ that the system follows from time $t = 0$ to $t = T$ [7]. In the continuous time the action integral is defined as

$$S = \int_0^T L(q, \dot{q}) \, dt \,. \tag{11}$$

Hamilton's principle states that the actual path followed by a holonomic system results in a stationary action integral with respect to path variations for fixed endpoints. Taking the variation of Eq. (11) gives

$$\delta S = \int_0^T \frac{\partial L}{\partial q} - \frac{d}{dt}\left(\frac{\partial L}{\partial \dot{q}}\right) \, dt \,, \tag{12}$$

where we have used integration by parts and the conditions $\delta q(0) = 0$ and $\delta q(T) = 0$. For Hamilton's principle to be valid for all admissible variations δq, the integrand of Eq. (12) must be zero for all t, giving the continuous Euler-Lagrange Equations [16].

$$0 = \frac{\partial L}{\partial q} - \frac{d}{dt}\left(\frac{\partial L}{\partial \dot{q}}\right) \,. \tag{13}$$

Hamilton's equations are derivable through the use of the Legendre transformation which is a mapping $(q, \dot{q}, t) \to (q, p, t)$ where p_i is the generalized momenta.

$$p_i = \frac{\partial L}{\partial \dot{q}_i} \,. \tag{14}$$

In the continuous time case the Hamiltonian is defined as

$$H = \sum_{i=1}^n p_i \dot{q}_i - L(q, \dot{q}, t) \,. \tag{15}$$

Applying Eq. (14) and taking the variation of Eq. (15) allows us to derive the equations of motion in Hamiltonian form

$$\dot{q}_i = \frac{\partial H}{\partial p_i} \,, \tag{16a}$$

$$\dot{p}_i = -\frac{\partial H}{\partial q_i} \,, \tag{16b}$$

$$\frac{\partial L}{\partial t} = -\frac{\partial H}{\partial t} \,. \tag{16c}$$

Both Eqs. (13) and (16) result in equations of motion for the mechanical system and are equivalent via the Legendre transform. Equation (13) results in n second order differential equations while Eq. (16) results in $2n$ first order differential equations.

3.2 Discrete Variational Mechanics

A discrete analogue of Hamilton's principle and the action integral is formed. Rather than taking a position, q, and velocity, $\dot{q}$, consider two positions q_0 and q_1 and a fixed time step $h \in \mathbb{R}$. The two positions are points on the curve $q(t)$ such that $q_0 \approx q(0)$ and $q_1 \approx q(h)$. A discrete time Lagrangian $L_d(q_0, q_1)$ is formed which approximates the action integral between q_0 and q_1 as

$$L_d(q_0, q_1) \approx \int_0^h L(q, \dot{q})\, dt\,. \tag{17}$$

Since Eq. (17) is calculated as a numerical integral, an appropriate quadrature rule is required. There are multiple possible methods one can use to approximate the integral in Eq. (17). An appropriate approximation rule is determined based on the ease of implementation and accuracy desired. Table 1 shows several possible

Table 1: Selected Quadrature Rules

Rectangle	$L_d(q_0, q_1) = L(q_0, \frac{q_1 - q_0}{h})h$
Midpoint	$L_d(q_0, q_1) = L(\frac{q_0 + q_1}{2}, \frac{q_1 - q_0}{h})h$
Trapezoidal	$L_d(q_0, q_1) = \frac{1}{2}\left[L(q_0, \frac{q_1 - q_0}{h}) + L(q_1, \frac{q_1 - q_0}{h})\right]h$

approximation rules that are typically applied. The rectangle rule is a first order accurate method and offers a straightforward implementation. The midpoint and trapezoidal rules are both second order accurate methods. However, the midpoint rule results in an implicit form which adds further complexity to the equations of motion.

Once an appropriate discrete Lagrangian is formed a discrete action sum is formed as the discrete analogue of Eq. (11)

$$S_d = \sum_{k=0}^{N-1} L_d(q_k, q_{k+1})\,. \tag{18}$$

Once again a discrete version of Hamilton's principle is applied to Eq. (18). This yields a discrete time counterpart to Eq. (12) as

$$\delta S_d = \sum_{k=1}^{N-1}\left[\frac{\partial L_d(q_k, q_{k+1})}{\partial q_k} + \frac{\partial L_d(q_{k-1}, q_k)}{\partial q_{k+1}}\right]\delta q_k\,. \tag{19}$$

For the discrete action sum to be stationary with respect to all admissible path variations, with fixed endpoints, the discrete Euler-Lagrange equations must be satisfied for $k = 1, \cdots, N-1$ resulting in

$$0 = \frac{\partial L_d(q_k, q_{k+1})}{\partial q_k} + \frac{\partial L_d(q_{k-1}, q_k)}{\partial q_{k+1}}\,. \tag{20}$$

A discrete version of the Legendre transformation, referred to as a discrete fiber derivative, results in the equivalent Hamiltonian form expression. The discrete fiber derivative is given as

$$p_k = \frac{\partial L_d(q_{k-1}, q_k)}{\partial q_{k+1}} = -\frac{\partial L_d(q_k, q_{k+1})}{\partial q_k} \, , \tag{21a}$$

$$p_{k+1} = \frac{\partial L_d(q_k, q_{k+1})}{\partial q_{k+1}} \, . \tag{21b}$$

This yields a discrete Hamiltonian map $(q_k, p_k) \rightarrow (q_{k+1}, p_{k+1})$. A more extensive development of variational integrators can be found in [21].

3.3 Discrete Equations of Motion

The discrete equations of motion for the PCRTBP are derived by choosing an appropriate quadrature rule to discretize the Lagrangian in Eq. (2). In this work, the trapezoidal approximation is applied. The trapezoid rule allows for an explicit second order accurate approximation. The discrete Lagrangian is given by

$$\begin{aligned} L_d = \frac{h}{2} \Bigg(&\frac{1}{2} \left[\left(\frac{x_{k+1} - x_k}{h} - y_k \right)^2 + \left(\frac{y_{k+1} - y_k}{h} + x_k \right)^2 \right] + \frac{1-\mu}{r_{1_k}} + \frac{\mu}{r_{2_k}} \\ &+ \frac{1}{2} \left[\left(\frac{x_{k+1} - x_k}{h} - y_{k+1} \right)^2 + \left(\frac{y_{k+1} - y_k}{h} + x_{k+1} \right)^2 \right] + \frac{1-\mu}{r_{1_{k+1}}} + \frac{\mu}{r_{2_{k+1}}} \Bigg) \, . \end{aligned} \tag{22}$$

Applying a discrete version of the Lagrange-d'Alembert principle allows for inclusion of an external control force on the system [21]. Using Eqs. (21) and (22) and some manipulation, the equations of motion are given by

$$x_{k+1} = \frac{1}{1+h^2} \left[h\dot{x}_k + h^2 \dot{y}_k + x_k \left(1 + \frac{3h^2}{2} \right) + \frac{h^3}{2} y_k - \frac{h^3}{2} U_{y_k} - \frac{h^2}{2} U_{x_k} \right] \, , \tag{23a}$$

$$y_{k+1} = h\dot{y}_k + hx_k - hx_{k+1} + y_k + \frac{h^2 y_k}{2} - \frac{h^2}{2} U_{y_k} \, , \tag{23b}$$

$$\dot{x}_{k+1} = \dot{x}_k - 2y_k + 2y_{k+1} + \frac{h}{2} \left(x_{k+1} + x_k \right) - \frac{h}{2} U_{x_{k+1}} - \frac{h}{2} U_{x_k} + hu_x \, , \tag{23c}$$

$$\dot{y}_{k+1} = \dot{y}_k + 2x_k - 2x_{k+1} + \frac{h}{2} \left(y_{k+1} + y_k \right) - \frac{h}{2} U_{y_{k+1}} - \frac{h}{2} U_{y_k} + hu_y \, . \tag{23d}$$

The discrete equations of motion are given in the Lagrangian form after applying the discrete fiber derivative from Eq. (21) as $p_{x_k} = \dot{x}_k - y_k$ and $p_{y_k} = \dot{y}_k + x_k$. The state is defined as $\boldsymbol{x}_k = \begin{bmatrix} x_k & y_k & \dot{x}_k & \dot{y}_k \end{bmatrix}^T$ and the control input is $\boldsymbol{u} = \begin{bmatrix} u_x & u_y \end{bmatrix}^T$. This results in a discrete update map $f_k : \boldsymbol{x}_k \rightarrow \boldsymbol{x}_{k+1}$ which preserves the same properties of the continuous-time dynamics in Eq. (7) such as invariants, symplecticity, and the configuration manifold. The discrete potential gradients are

given by

$$U_{x_k} = \frac{(1 - \mu)(x_k + \mu)}{r_{1_k}^3} + \frac{\mu(x_k - 1 + \mu)}{r_{2_k}^3}, \tag{24a}$$

$$U_{y_k} = \frac{(1 - \mu)y_k}{r_{2_k}^3} + \frac{\mu y_k}{r_{2_k}^3}, \tag{24b}$$

$$U_{x_{k+1}} = \frac{(1 - \mu)(x_{k+1} + \mu)}{r_{1_{k+1}}^3} + \frac{\mu(x_{k+1} - 1 + \mu)}{r_{2_{k+1}}^3}, \tag{24c}$$

$$U_{y_{k+1}} = \frac{(1 - \mu)y_{k+1}}{r_{1_{k+1}}^3} + \frac{\mu y_{k+1}}{r_{2_{k+1}}^3}. \tag{24d}$$

The distances to each primary are defined as

$$r_{1_k} = \sqrt{(x_k + \mu)^2 + y_k^2}, \tag{25a}$$

$$r_{2_k} = \sqrt{(x_k - 1 + \mu)^2 + y_k^2}, \tag{25b}$$

$$r_{1_{k+1}} = \sqrt{(x_{k+1} + \mu)^2 + y_{k+1}^2}, \tag{25c}$$

$$r_{2_{k+1}} = \sqrt{(x_{k+1} - 1 + \mu)^2 + y_{k+1}^2}. \tag{25d}$$

Care must be taken during the implementation of Eq. (23). As Eqs. (24) and (25) are defined at both step k and $k + 1$ they must be evaluated at both time instances. Equation (23) is implemented by first defining an initial state $\boldsymbol{x}_k$ and control $\boldsymbol{u}_k$. The distances and gravitational potential at step k are evaluated from Eqs. (24a), (24b), (25a) and (25b). The discrete update steps in Eqs. (23a) and (23b) are evaluated to generate x_{k+1} and y_{k+1}. Next, the distances and gravitational potential at step $k + 1$ are evaluated from Eqs. (24c), (24d), (25c) and (25d). Finally, the update steps in Eqs. (23c) and (23d) are evaluated. This results in the complete discrete update map $\boldsymbol{x}_k \to \boldsymbol{x}_{k+1}$ given $\boldsymbol{u}_k$.

3.4 Numerical Example

A simulation comparing the variational integrator to a conventional Runge-Kutta method is given in Fig. 2. A particle is simulated from an initial condition of $\boldsymbol{x}_0 = \begin{bmatrix} 0.75 & 0 & 0 & 0.2883 \end{bmatrix}^T$ for $t_f = 200 \approx 15$ years in the Earth-Moon system. The variational integrator uses a step size of $47.22\,\mathrm{s}$ while the Runge-Kutta method uses a variable step size implemented via ODE45 in Matlab. Figure 2a shows the trajectory of the spacecraft in the rotating reference frame for both integration schemes. Both integration schemes result in trajectories that are initially nearly identical. The discrete equations of motion are an accurate approximation for the continuous dynamics as they closely match the solution of ODE45 over the initial portion of the simulation. However, as time progresses the trajectories begin to diverge due to the differences in system energy. Figure 2b shows the evolution of the Jacobi integral. The variational integrator exhibits a bounded behavior about the initial energy with a mean variation of 4.2522×10^{-20}. However, the conventional Runge-Kutta method demonstrates a clear energy drift of 4.2814×10^{-8}. Over long simulation horizons or with the addition of small control inputs this poor energy behavior limits the applicability of conventional techniques.
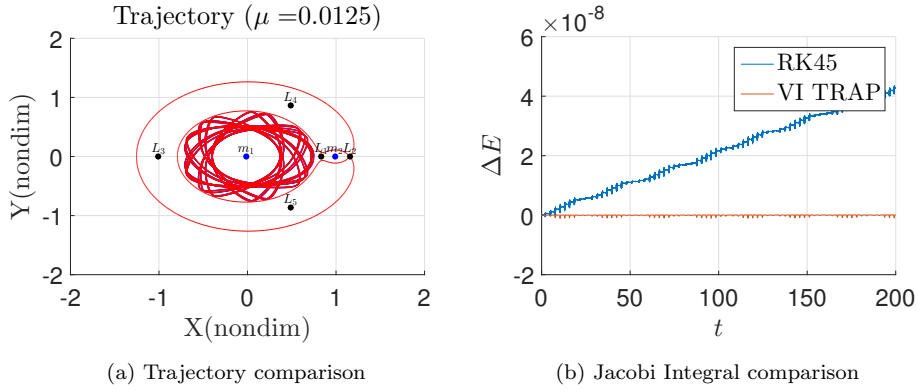
(a) Trajectory comparison

(b) Jacobi Integral comparison

Fig. 2: Integrator Comparison

4 Invariant Manifolds and Poincaré Map

Dynamics systems theory has been applied to design control-free maneuvers in the restricted three-body problem [15]. As previously introduced in Section 2.1, there exist five equilibrium points in the equations of motion for the three-body problem. It has been shown that the local orbit structure near the Lagrange points gives rise to families of periodic orbits as well as the stable and unstable manifolds of these periodic orbits. This rich structure is globally connected and gives rise to a dynamical chain which allows trajectories to pass through the phase space [15, 4]. The manifold structure associated with periodic orbits about the L_1 and L_2 Lagrange points are critical to the understanding of the motion of spacecraft as well as comets/asteroids. In addition, the stable and unstable manifolds serve as the boundaries of the phase space region that allow for the transport between realms in a single three-body system or between multiple three-body systems. These invariant manifolds only exist as a result of the dynamic formulation of the three-body problem in a rotating reference frame.

4.1 Invariant Manifolds

Invariant manifolds serve as a higher dimensional generalization of the concept of seperatrices from linear systems as applied to the case of nonlinear systems. To compute these manifolds first one must determine an appropriate periodic orbit. The process of differential correction and numerical continuation are used to determine a periodic orbit with a desired energy level. Let the trajectories of the equations of motion defined in Eq. (7) be defined by the flow map $\phi(t; \boldsymbol{x}_0)$ originating from $\boldsymbol{x}(t_0) = \boldsymbol{x}_0$ and we define a periodic orbit as γ. The invariant manifolds are defined as :

$$W^s(\boldsymbol{x}_0) = \{\boldsymbol{x} : \phi(t; \boldsymbol{x}_0) \to \gamma \text{ as } t \to \infty\},$$
$$W^u(\boldsymbol{x}_0) = \{\boldsymbol{x} : \phi(t; \boldsymbol{x}_0) \to \gamma \text{ as } t \to -\infty\}.$$

The stable manifold, $W^s(\boldsymbol{x}_0)$, is the set of trajectories which asymptotically approach the periodic orbit. Similarly, the unstable manifold, $W^u(\boldsymbol{x}_0)$, is the set
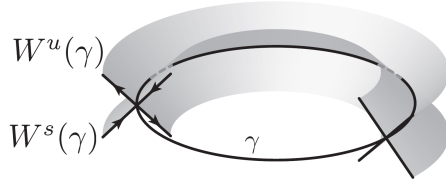
Fig. 3: Stable and unstable manifold of a periodic orbit

of trajectories which asymptotically depart the periodic orbit. For the nonlinear system, defined by Eq. (7) or Eq. (23), we can determine the state transition matrix Φ along the periodic orbit, from $0 \to T$, by numerical integration of the variational equations. In the neighborhood of the periodic orbit γ, the tangent spaces to the stable and unstable manifolds are provided by the generalized eigenspaces E^s and E^u of the linearization $A = \mathbf{D}f(\boldsymbol{x}_0)$, where $\boldsymbol{x}_0$ is on the periodic orbit. The eigenvectors of the monodromy matrix, $M = \Phi(T)$, serve to locally approximate the directions of the stable and unstable manifolds. A perturbation in the direction of the unstable eigenvector, with $\|\lambda\| > 1$, is used to generate an initial condition on the unstable manifold. Similarly, a perturbation in the direction of the stable eigenvector, with $\|\lambda\| < 1$, is used to generate an initial condition on the stable manifold. Each periodic orbit has two stable and unstable manifold sets associated with both a positive or negative perturbation along the respective eigenvector. This technique of determining the invariant manifolds is graphically presented in Fig. 3.

Poincaré maps are a useful tool in the analysis of the flow near periodic orbits in the three-body problem. We let Σ define a hypersurface of section chosen such that all trajectories in the vicinity of a state $\boldsymbol{q} \in \Sigma$ cross Σ transversely and in the same direction. A Poincaré map, $P(\boldsymbol{q}) = \phi(T; \boldsymbol{q})$, maps the state of a trajectory from one intersection to the next. Choosing a section in this manner results in a Poincaré section as shown in Fig. 4. This allows for greater insight into the stability and dynamics of periodic solutions of a dynamic system as a fixed point on the Poincaré section corresponds to a periodic orbit while movement on the section is associate with the stability of neighboring trajectories. For example, Poincaré maps have been used to prove the existence of homoclinic orbits, which are orbits both forward and backward asymptotic to a single unstable periodic orbit, and heteroclinic orbits, which join different periodic orbits [4,14]. These dynamic features have been shown to play a vital role in the movement of natural bodies as well as critical for spacecraft missions [5,18].

4.2 Control-free Orbital Transfers

Combining invariant manifolds and an appropriate Poincaré section provides a conceptually simple manner to determine trajectories which connect wide regions of the phase space. Figure 5 demonstrates how a Poincaré map may be used to determine a connection between periodic orbits. The initial orbit is a planar periodic orbit about L_2 in the Earth-Moon system while the final orbit is a periodic orbit about L_1. Both periodic orbits have the same Jacobi energy constant and as
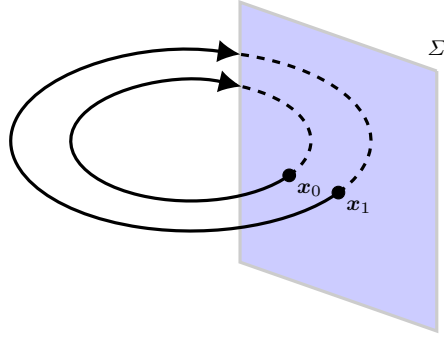
Fig. 4: Diagram of the Poincaré map

a result it is possible to transfer between the orbits without any energy change. Figure 5a shows the unstable manifold of the initial orbit and the stable manifold of the desired orbit. Both invariant manifolds are globalized and propogated to the first intersection with the Poincaré surface of section located at the position of the Moon, $x = 1 - \mu$. The Poincaré section in Fig. 5 is defined as

$$\Sigma = \{(y, \dot{y}) \,|\, x = 1 - \mu, y > 0\} ,$$

and located to allow an intersection between both invariant manifolds. The configuration space of the invariant manifold is $\boldsymbol{x} \in \mathbb{R}^4$. The surface of section, and the resulting intersection of the four-dimensional space with the hyperplane Σ, reduces the resulting intersection to a surface in $\mathbb{R}^3$. Since the two orbits share the same Jacobi constant, the intersection phase space is further reduced to $\mathbb{R}^2$. The intersection of the invariant manifolds on the Poincaré section is central to determining transfer connections between the initial and final orbits.

The position, y, and velocity, $\dot{y}$, at the Poincaré section are plotted in Fig. 5b. The surface of section is placed at a strategic location in order to allow for a cross section of the flow within the three-dimensional energy surface. In a frame aligned with the rotating frame, $(\hat{\boldsymbol{e}}_1, \hat{\boldsymbol{e}}_2)$, but centered on the equilibrium point L_1 or L_2, the unstable manifolds are locally moving in forward time in the second and forth quadrant. Similarly, the stable manifold branches are locally moving in backward time in the first and third quadrants as illustrated in Fig. 3. As a result, the location of the section in Fig. 5b is chosen to intersect both the stable manifolds of L_1 periodic orbits as well as unstable manifolds of L_2 periodic orbits. Additional Poincaré sections are located at other heteroclinic points in the phase space to enable design throughout the phase space [15]. In this way, it is possible to design trajectories that intersect the invariant manifolds and connect widely separated regions of the state space. This technique has been heavily investigated in [15], applied to operational missions in [13], and applied to potential multi-moon orbiter missions in [28]. In addition, much recent work has focused on potential return missions to the Moon [30, 2, 23, 24, 22].

However, the results previously developed are highly case specific and difficult to generalize to arbitrary transfers. Also, these results are based on control-free trajectories which rely on the underlying structure of the three-body system. In addition, transfer orbits along an invariant manifold require large time of flights

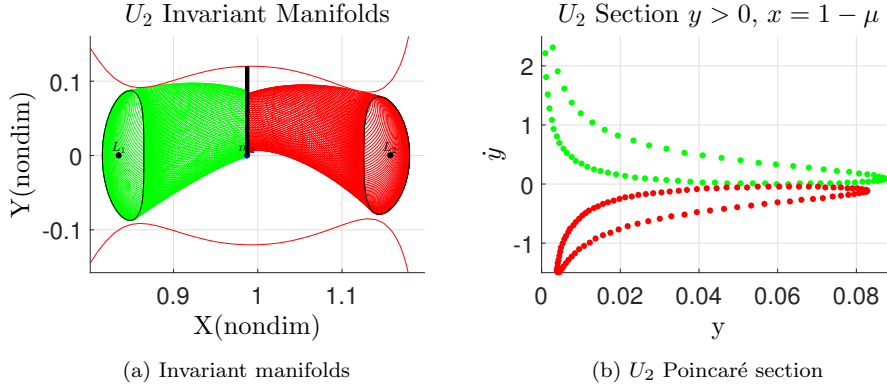(a) Invariant manifolds   (b) U_2 Poincaré section

Fig. 5: Illustration of process to identify transfer trajectories

which may be undesirable for time critical missions. The addition of low-thrust propulsion offers the potential of reduced transit times and the ability to depart from the free motion trajectory to allow for increased transfer opportunities. In this paper, we formulate an optimal control problem to generate the reachable set of the spacecraft. We compute the reachable set on an appropriate Poincaré section and use this to design a transfer trajectory.

5 Optimal Control Formulation for Reachability Set

In this section, an optimal control formulation is presented to determine and design transfers within the three-body problem. The application of variational integrators to optimal control problems is referred to as computational geometric optimal control. Our formulation is based on the concept of the reachability set on a Poincaré section. This method allows one to easily determine potential transfer opportunities by finding set intersections on a lower dimensional space and greatly reduces the design process. The addition of continuous low thrust propulsion extends the control free design process developed previously and allows for a greater range of potential transfers with a reduced time of flight.

5.1 Reachability Set

Reachability theory provides a framework to evaluate control capability and safety. The reachable set contains all possible trajectories that are achievable over a fixed time horizon from a defined initial condition, subject to the operational constraints of the system. Reachability theory has been applied to aerospace systems such as collision avoidance, safety planning, and performance characterization. The theory formally supporting reachability has been extensively developed and is directly derivable from optimal control theory [29,19,20]. More recently, reachability theory has recently been applied to space systems [10,12]. Computation of the reachable set for a system involves solving the Hamilton-Jacobi partial differential equation or satisfying a dynamic programming principle. Analytical computation
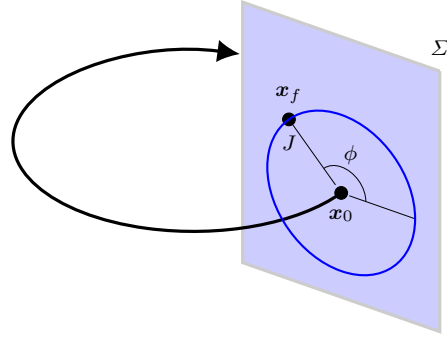
Fig. 6: Reachability set on a Poincaré section

of reachable sets is an ongoing problem and is only possible for certain classes of systems. Typically, numerical methods are used to generate approximations of the reachability set, but are generally limited by the dimensionality of the problem.

Computation of reachable sets is critical to space situational awareness, rendezvous and proximity operations, and orbit determination operations. Specifically, maintaining accurate estimates of a spacecraft state over extended periods is not trivial. The challenge is increased for multiple spacecraft operating in close proximity or when there are long periods of time between measurements. Coupling the ability for continuous low-thrust propulsion between measurements increases the measurement association complexity. Computing the reachability set given estimated states and control authorities allows one to better correlate subsequent measurements or determine sensor pointing regions in the event of a lost spacecraft.

5.2 Optimal Control Formulation

In this paper, we seek to approximate the reachability set on a Poincaré section by solving a related optimal control problem. We choose our Poincaré section in a similar manner to those used previously for the design of transfers via invariant manifolds. The Poincaré section is chosen to intersect transversally with trajectories emanating from the initial orbit. In the case of a periodic orbit the trajectories will cross the Poincaré section at two distinct fixed points every half period. The main idea is that the addition of low thrust propulsion allows us to enlarge the set of trajectories achievable in the Poincaré section. Figure 6 illustrates how, without any control input, trajectories will intersect with the Poincaré section at $\boldsymbol{x}_n$. However, the addition of low thrust propulsion allows the spacecraft to depart from the natural dynamics and intersect the Poincaré section at a different location. We use a cost function to define a distance metric on the Poincaré section from the control-free intersection to an intersection under the influence of the control input. Maximization of this distance along varying directions enables us to generate the largest reachability set under the bounded control input.

We define the Poincaré section along the horizontal axis, which is equivalent to the surface $y = 0$, and given by

$$\Sigma = \{(x, \dot{x}) \, | \, y = 0\} \, . \tag{26}$$

This is similar to the previous work in determining homoclinic orbits in the three-body problem [17, 15]. Previous analytical results have shown that homoclinic orbits intersect transversally in the $(x, \dot{x})$ space on the plane $y = 0$. We seek to compliment these results with the addition of low thrust propulsion to maximize the reachable set on the Poincaré section. Placing our section at $y = 0$ ensures that all trajectories will intersect our section. An optimal control problem is defined by a cost function

$$J = -\frac{1}{2} \left(\boldsymbol{x}(N) - \boldsymbol{x}_n(N) \right)^T \begin{bmatrix} 1 & 0 & 0 & 0 \\ 0 & 0 & 0 & 0 \\ 0 & 0 & 1 & 0 \\ 0 & 0 & 0 & 0 \end{bmatrix} \left(\boldsymbol{x}(N) - \boldsymbol{x}_n(N) \right) = \phi(\boldsymbol{x}(N), \boldsymbol{x}_n(N)) \, . \tag{27}$$

The term $\boldsymbol{x}_n(N)$ is the final state of a control-free trajectory while the term $\boldsymbol{x}(N)$ is the final state under the influence of the control input. Maximization of the distance between $\boldsymbol{x}_n$ and $\boldsymbol{x}$, on the Poincaré section defined in Eq. (26) at the terminal time $t_f = N$, is equivalent to the minimization of J defined in Eq. (27). The Poincaré section is defined through the use of appropriate terminal constraints given by

$$v_1(\boldsymbol{x}(N)) = y(N) = 0 \, , \tag{28a}$$

$$v_2(\boldsymbol{x}(N)) = \frac{\dot{x}(N) - \dot{x}_n(N)}{x(N) - x_n(N)} - \tan\theta_d = 0 \, , \tag{28b}$$

$$0 \geq \boldsymbol{u}^T \boldsymbol{u} - u_{max}^2 \, , \tag{28c}$$

where the angle θ_d defines a direction in which we wish to maximize the reachability set on the Poincaré section. The maximum control thrust magnitude is defined by u_{max} and is non-dimensionalized by the characteristic units of length, mass, and time. The goal is to determine the control input $\boldsymbol{u}_k$ such that the cost function Eq. (27) is minimized subject to the state equations of motion Eq. (23) and constraints Eq. (28).

Application of the Euler-Lagrange equations allows us to derive the necessary conditions for optimality [1]. The discrete variational integrator in Eq. (23) is used rather than the continuous time counterpart. This results in a discrete optimal control problem and the discrete necessary conditions are given as

$$\boldsymbol{\lambda}_{k+1}^T = \boldsymbol{\lambda}_k^T \left(\frac{\partial \boldsymbol{f}_k}{\partial \boldsymbol{x}_k} \right)^{-1} \, , \tag{29a}$$

$$0 = \frac{\partial H_k}{\partial \boldsymbol{u}_k} \, , \tag{29b}$$

$$0 = \frac{\partial \phi}{\partial \boldsymbol{x}_k}^T + \frac{\partial \boldsymbol{v}}{\partial \boldsymbol{x}_k}^T \boldsymbol{\beta} - \boldsymbol{\lambda}^T(N) \, , \tag{29c}$$

where the Hamiltonian H is defined as

$$H_k = \boldsymbol{\lambda}_k^T \boldsymbol{f}(\boldsymbol{x}_k, \boldsymbol{u}_k) \, , \tag{30}$$
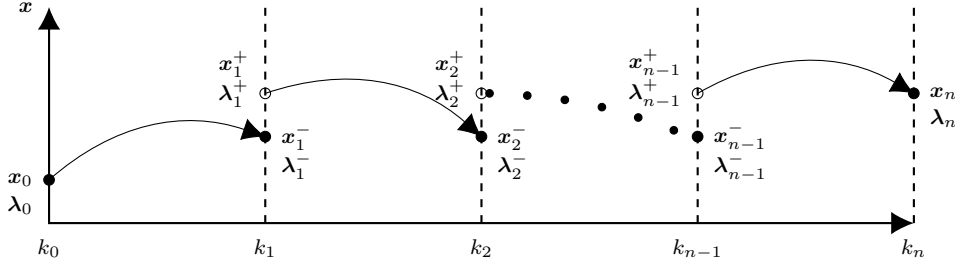
Fig. 7: Multiple Shooting method

and $\boldsymbol{\lambda} \in \mathbb{R}^{4 \times 1}$ is the costate and $\boldsymbol{\beta} \in \mathbb{R}^{2 \times 1}$ are the additional Lagrange multipliers associated with the terminal constraints in Eq. (28). The state dynamics are represented by $\boldsymbol{f}(\boldsymbol{x}_k, \boldsymbol{\lambda}_k)$ after substituting Eq. (29b) into Eq. (23). This indirect optimal control formulation leads to a two point boundary value problem with split boundary conditions. By sweeping the angle θ_d one can approximate the reachable set on the Poincaré section subject to the bounded control input.

The costate equation of motion requires the Jacobian of Eq. (23) and is given by

$$
\boldsymbol{\lambda}_{k+1}^T = \boldsymbol{\lambda}_k^T \begin{bmatrix} f_{1_x} & f_{1_y} & f_{1_{\dot{x}}} & f_{1_{\dot{y}}} \\ f_{2_x} & f_{2_y} & f_{2_{\dot{x}}} & f_{2_{\dot{y}}} \\ f_{3_x} & f_{3_y} & f_{3_{\dot{x}}} & f_{3_{\dot{y}}} \\ f_{4_x} & f_{4_y} & f_{4_{\dot{x}}} & f_{4_{\dot{y}}} \end{bmatrix}^{-1} .
\tag{31}
$$

The derivation of Eq. (31) is given in Appendix A. In addition, the computation of Eq. (31) requires inversion of the Jacobian matrix. This is a computationally expensive operation that is prone to numerical error and instability. A method is presented in Appendix B to avoid this inversion and determine an explicit update map $\boldsymbol{\lambda}_k \rightarrow \boldsymbol{\lambda}_{k+1}$.

The optimal control formulation presented in this section results in a two point boundary value problem (TPBVP). There exist many methods to solve TPBVPs such as gradient, quasilinearization, and shooting methods [1,11]. Shooting methods are common in astrodynamic trajectory design problems and relatively simple to implement. In the shooting method, initial conditions are varied such that a terminal constraint is satisfied, similar to the way an archer modifies the bow in order to more accurately strike a target. Consider the vector of initial conditions, $\boldsymbol{\chi} = \{\boldsymbol{x}_0, \boldsymbol{\lambda}_0\}$, which is varied to satisfy some terminal constraints of the form $\boldsymbol{G}(\boldsymbol{\chi}) = \{\boldsymbol{x}_t - \boldsymbol{x}_n\} = 0$. The free variables at the terminal time are computed by propogation of $\boldsymbol{\chi}$ over the selected time horizon. At the terminal time, the constraint vector is calculated and if not satisfied $\boldsymbol{\chi}$ is varied. Rather than numerical integration over the entire time interval, multiple shooting segments the interval into several smaller sub-arcs [26]. The multiple shooting method is implemented in this paper which alleviates many of the issues associated with single shooting approaches.

In Fig. 7, we show a schematic representation of the multiple shooting procedure. We split the optimal control horizon into equal length subsegments such that the length of each segment is $\frac{k}{n}$, where k, n are the total number of steps and number

of stages, respectively. Similarly, we divide the state and costate trajectories into n equal segments. To ensure continuity, additional interior constraints are incorporated as

$$\boldsymbol{x}_1^- - \boldsymbol{x}_1^+ = 0, \tag{32a}$$

$$\boldsymbol{\lambda}_1^- - \boldsymbol{\lambda}_1^+ = 0, \tag{32b}$$

$$\boldsymbol{x}_2^- - \boldsymbol{x}_2^+ = 0, \tag{32c}$$

$$\boldsymbol{\lambda}_2^- - \boldsymbol{\lambda}_2^+ = 0, \tag{32d}$$

$$\vdots \tag{32e}$$

$$\boldsymbol{x}_{n-1}^- - \boldsymbol{x}_{n-1}^+ = 0, \tag{32f}$$

$$\boldsymbol{\lambda}_{n-1}^- - \boldsymbol{\lambda}_{n-1}^+ = 0. \tag{32g}$$

Using the multiple shooting method reduces the sensitivity of the terminal states, $\boldsymbol{x}_i^+, \boldsymbol{\lambda}_i^+$, to variations of the initial states, $\boldsymbol{x}_{i-1}^-, \boldsymbol{\lambda}_{i-1}^-$. As a result, the design vector $\boldsymbol{\chi}$ is augmented with the additional interior initial conditions, $\boldsymbol{x}_i^-, \boldsymbol{\lambda}^-$. Similarly, the constraint vector is augmented with the additional interior constraints defined in Eq. (32a). The multiple shooting algorithm now varies the design vector $\boldsymbol{\chi}$ to ensure that the constraints in $\boldsymbol{G}(\boldsymbol{\chi})$ are satisfied. In this work, we use the Matlab nonlinear solver `fsolve` to solve the system of nonlinear equations defined by the multiple shooting algorithm.

6 Numerical Example

We present two numerical simulations in the Earth-Moon system to demonstrate the transfer procedure. These simulations enable the spacecraft to depart from the natural dynamics through the use of low-thrust propulsion. The reachability set on the Poincaré section allows for a straightforward method of determining transfer opportunities.

6.1 Periodic Orbit transfer

The first objective is to design a transfer trajectory from a planar periodic orbit about the L_1 Lagrange point to a bounded orbit in the vicinity of the Moon. The target region is created by choosing an initial condition of $x_0 = \begin{bmatrix} 1.05 & 0 & 0 & 0.35 \end{bmatrix}^T$ with $\mu = 0.0125$. The target set is propagated over a period of $t = 20$ in non-dimensional units which corresponds to approximately 1.5 years. Figure 8 shows that the target set remain in the vicinity of the Moon, or m_2, in the rotating reference frame. This type of orbit would be useful for a variety of mission scenarios. For example, a series of communication satellites could be placed in this type of orbit. The bounded trajectories of the vehicles and constant line of sight to both the Moon and the Earth would allow for constant communication for future manned missions and potential habitats. The initial set is a planar periodic orbit about L_1. We generate the periodic orbit by using a linear approximation to first determine periodic solutions. This approximate periodic solution from the linear system is
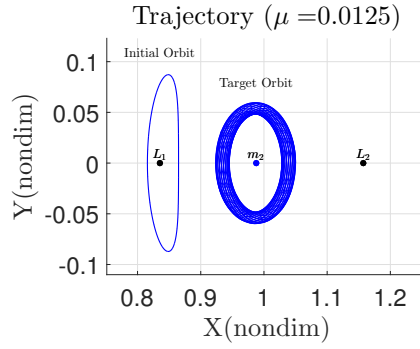
Fig. 8: Target Orbit Region

then implemented in the nonlinear dynamics through the method of differential correction, or single shooting [15]. The initial $\dot{y}$ is varied until the the periodic orbit makes a perpendicular crossing, $\dot{x} = 0$, after one half period. Due to the symmetry of the three-body problem, this ensures that the trajectory will return to the initial state after a single period.

As a source for comparison, the method of using invariant manifolds, introduced in [15], is implemented. As described in Section 4.1, these invariant manifolds are the set of trajectories that either asymptotically arrive or depart the periodic orbit. We generate the unstable manifold associated with the initial planar periodic orbit. We numerically propagate the unstable manifold forward in time until the trajectories intersect the Poincaré section $y = 0$. Figure 9a shows the unstable invariant manifold generated from the initial L_1 periodic orbit. The blue points in Fig. 9b are the intersections of the target Moon orbit and the Poincaré section. The two circular regions are the ascending (right) and descending (left) intersections of the target orbit and Poincaré section. The green points in Fig. 9b are intersections of the unstable manifold from Fig. 9a with the Poincaré section $y = 0$. Only a single branch of the invariant manifold intersects with the ascending region of the target orbit. There are no intersections of the invariant manifold with the descending region of the target orbit. The numerical values associated with the green points denote the required time of flight along the invariant manifold in non-dimensional units. The required travel time for a transfer using the unstable invariant manifold is $t_f \approx 3.1$.

Next, we determine the reachability set with the addition of a low thrust control input. We define a maximum magnitude of the thrust as $u_{max} = 0.75$ and assume we can point the thrust in any direction within the plane. This model is representative of many spacecraft which have a body fixed thruster and attitude control system. We assume a fully actuated spacecraft model which decouples the translational and rotational dynamics. The trajectories are generated from a fixed initial state of $\boldsymbol{x}_0 = \begin{bmatrix} 0.8156 & 0 & 0 & 0.1922 \end{bmatrix}^T$ over a fixed time span of $t_f = 1.4$. This initial state lies on the initial periodic orbit and the time of flight is equivalent to one half period of the initial periodic orbit.

From the initial state on the periodic orbit, a series of optimal trajectories are generated to determine the reachable set. The multiple shooting approach is implemented to solve the optimal control problem. We divide the time horizon
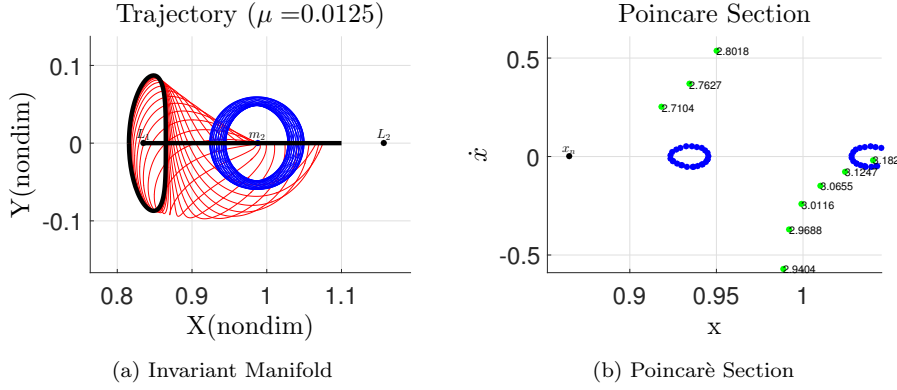
(a) Invariant Manifold

(b) Poincarè Section

Fig. 9: Invariant manifold transfer

into two equal length segments. The state trajectory is intialized using the free trajectory of the periodic orbit. Similarly, the costate trajectory is initialized from an initial guess of $\boldsymbol{\lambda}_0 = \begin{bmatrix} -1 & -1 & -1 & -1 \end{bmatrix}^T$ and propogated using the discrete equations of motion in Eq. (46). This results in the initial guess of the design vector $\boldsymbol{\chi} = \begin{bmatrix} \boldsymbol{\lambda}_0 & \boldsymbol{x}_1^- & \boldsymbol{\lambda}_1^- & \boldsymbol{\beta} \end{bmatrix}^T$. This design vector is then varied to ensure that the necessary conditions of optimality and the interior point constraints are satisfied.

By varying the angle θ_d in Eq. (28), a different direction along the Poincaré section is maximized. We discretely vary the angle over the range $0° \leq \theta_d < 360°$ to approximate the reachability set of the spacecraft. Choosing a new angle θ_d corresponds to a different direction as well as a new optimal control problem which is again solved using the multiple shooting approach laid out previously. The intersection of the optimal trajectories as well as those of the target Moon orbit with the Poincaré section are shown in Fig. 9.

The optimal trajectories, under the influence of the control input $\boldsymbol{u}$, are plotted in red in Fig. 10a. Initially, the spacecraft is assumed to lie on the periodic orbit. As a result, the intersection of this periodic orbit with the Poincaré section are two points corresponding to the two crossing of the orbit. We show the control-free intersection, $\boldsymbol{x}_n$, of the periodic orbit on the Poincaré section in Figs. 9b and 10b The use of the continuous low thrust propulsion expands the reachable set to region bounded by the red markers in Fig. 10b. The reachable set is an ellipsoidal region with a major axis aligned along $\theta \approx 70°$ as compared to a fixed point without any control input.

Figure 10b shows that the reachable set and those of the descending target region intersect. As both regions are discretely approximated a linear interpolation is used to determine the exact intersection state on the Poincaré section. This intersection generates a partial target state of x_t and $\dot{x}_t$. Using the energy level of the target region, defined by Eq. (10), and the intersection state we can calculate the final component $\dot{y}$ is calculated. This results in a complete target state $\boldsymbol{x}_t$ which lies on the reachable set and on the target orbit. A final optimal trajectory is generated such that the $\boldsymbol{x}(N) = \boldsymbol{x}_t$. This transfer trajectory is denoted by the green path in Fig. 10c. The optimal control input is shown in Fig. 10d. The spacecraft achieves the desired target while satisfying the bounded control input.

(a) Reachability set trajectories

(b) Poincaré section
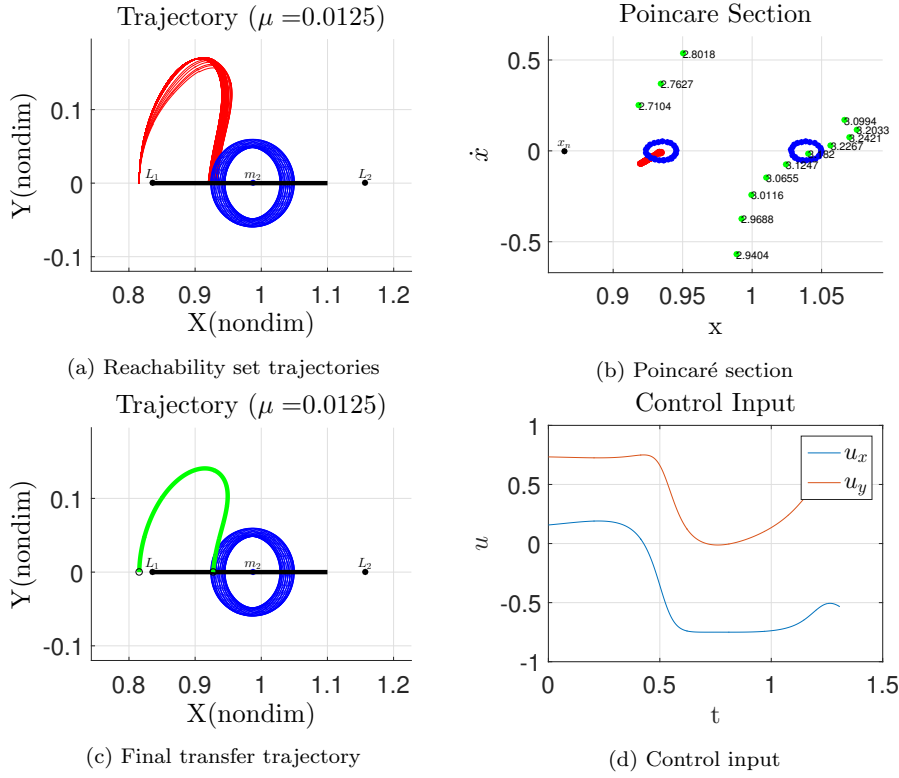

(c) Final transfer trajectory

(d) Control input

Fig. 10: Reachability set transfer

A transfer along the invariant manifold requires on average $t_f \approx 3.1$ as compared to $t_f \approx 1.4$ for a transfer using low thrust propulsion and the reachable set. This long time of flight is typical of transfers using invariant manifolds. The unstable invariant manifold traverses a large region of the phase space and is dependent on the system dynamics. In addition, the invariant manifolds asymptotically arrive and depart from the periodic orbit. As a result, it may take an arbitrarily long period of time to depart from the vicinity of the periodic orbit. In addition, only a small portion of the invariant manifold intersects with the target Moon orbit. In contrast, the low thrust control input we are able to enlarge the reachability set from a single point to a larger ellipsoidal region in Fig. 10b. This achieves an intersection with the target orbit with a much lower time of flight as compared to the invariant manifold method. In addition, by generating the reachability set we are able to compute the required control input to exactly intersect the target orbit. This avoids having to compute and accomplish a secondary impulsive manuever to transition from the invariant manifold to the target orbit.

6.2 Geostationary Transfer

There are many situations where a more complicated and extensive orbital transfer is desired. For example, we present a simulation of transferring from a geostationary orbit to the a periodic orbit about the Moon. This type of low energy transfer would be most suitable for unmanned spacecraft transitioning from the Earth to the Moon. The long time of flight would make such a transfer unsuitable for manned missions due to life support constraints. Future proposals for permanent lunar spacecraft and bases will require frequent supply missions to remain viable. Low energy transfers from the Earth to the Lagrange points are necessary for future missions.

The previous example demonstrated the capability of determining an orbital transfer after determining the intersection of the reachability set and a target orbit. However, it may not be possible to achieve an intersection on the Poincaré section after a single iteration. Since the spacecraft has an upper bounded control input and time of flight the reachability set is finite in size. As a result, we present a method of performing several iterations of the reachability set computation. A straightforward method is presented which allows for a series of reachability sets to be computed which progressively move the trajectory towards the target. In this manner, it is possible to determine more complicated transfers by a simple selection of states from the reachability set.

It is possible to design arbitrary transfers using either a direct optimization or invariant manifold based approach. The direct optimization method transforms the optimal control problem into a nonlinear programming problem. Instead of solving the Euler-Lagrange equations the state and control histories are parameterized and solved through any number of mathematical programming methods. However, due to this parameterization only an approximate solution, which approximates the true optimal solution in the limit, is feasible. On the other hand, our method applies an indirect optimization method. The necessary conditions for optimality are computed and directly solved in generating the reachability set. The use of the reachability set also avoids the issues of selecting a valid initial condition. We select a state on the maximum reachability set which minimizes the distance toward the target. This straightforward approach achieves an optimal trajectory and is used to generate general transfers.

The invariant manifold method is difficult to apply to general orbital transfers. The manifolds are associated with periodic orbits in the three-body system. In this case, an appropriate periodic orbit must first be determined prior to generating the invariant manifold. Furthermore, there is no guarantee that the invariant manifold will pass through a desired region of space. For example, in the Earth-Moon system the unstable manifolds of periodic orbits about L_1 do not pass close to the Earth, but rather are beyond the geostationary orbit altitude. In addition, determining the intersections between various invariant manifolds is not trivial. It requires an appropriate Poincaré section and the generation of several invariant manifolds. There is no clear method of selecting the periodic orbits required based on a the type of transfer desired. Determining an intersection between these invariant manifolds generally requires extended flight times, involving several orbits of the primaries, before an appropriate intersection is found. As a result, it is difficult to generalize this method to arbitrary transfers in the three-body problem.

This numerical simulation demonstrates the ability of the proposed approach. We use multiple iterations of the reachability set to achieve a more complicated transfer. In this manner, it is possible to design arbitrary transfers which are not possible using a single reachability computation. Initially, it is assumed that the spacecraft lies on a circular geostationary orbit in the non-dimensional Earth-Moon three-body system. The geostationary orbit about the Earth is transformed into the rotating reference frame of the Earth-Moon three body problem. In addition, we nondimensionalize the initial state to find $\boldsymbol{x}_0 = \begin{bmatrix} 0.0972 \ 0 \ 0 \ 3.0010 \end{bmatrix}^T$ as the initial condition of the spacecraft on the geostationary orbit. It is desired to transfer to a periodic orbit about the L_1 Lagrange point. The periodic orbit is defined by the initial condition $\begin{bmatrix} 0.8057 \ 0 \ 0 \ 0.2982 \end{bmatrix}$. The initial and target orbits are illustrated in Fig. 11. In order to effectively utilize the dynamics of the three-body system the
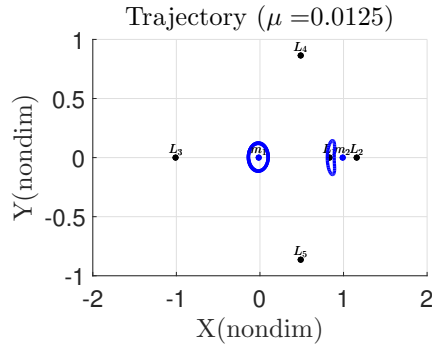

Fig. 11: Transfer target

stable manifold of the periodic orbit is targeted. We seek to generate a transfer from the geostationary orbit onto the stable invariant manifold. Once on the manifold, the spacecraft will coast in an uncontrolled fashion and asymptotically arrive at the desired periodic orbit.
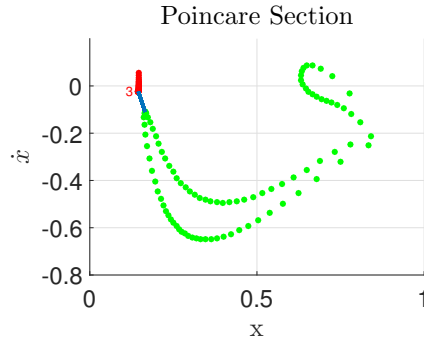

Fig. 12: Reachable set after three iterations

Next, we generate the stable invariant manifold associated with the periodic orbit in order to determine our target set. The stable manifold is propagated to the Poincaré section at $y = 0$, which is denoted by the horizontal black line in Fig. 13a. Next, we compute the reachable sets originating on the geo-stationary orbit and subject to the maximum control constraint. The multiple shooting approach is used to solve the optimal control problem with two segments. For the first reachability set computation, the initial geostationary orbit is used to initialize the multiple shooting algorithm. We use the same initial guess of $\boldsymbol{\lambda}_0$ as in Section 6.1 and propogate over the fixed time horizon of the period of the geostationary orbit to initialize $\boldsymbol{\lambda}_i^-$.

The first reachable set is computed beginning on the geostationary orbit at it's intersection with the Poincaré section and we again assume a upper bound on the thrust magnitude of $u_{max} = 0.75$. The reachable set is generated by varying the angle $0° \leq \theta < 360°$ in Eq. (28) defined on the Poincaré section. This allows us to approximate the set of states that are achievable in the $(x, \dot{x})$ space. After each computation of the reachability set we pick a state which minimizes the distance on the Poincaré section towards the stable manifolds as the function d

$$d(\boldsymbol{x}(N)) = \sqrt{(x - x_t)^2 + (\dot{x} - \dot{x}_t)^2}.$$

From the reachable set, the trajectory which minimizes d is used to intialize the next iteration. Once the reachability set intersects the stable manifold, we can achieve a complete transfer from the initial geostationary orbit to the stable manifold of L_1. For example, Fig. 12 shows the reachable set after three iterations in red and the minimum distance to the stable manifold in green. The state and costate trajectories associated with this point on the rechable set is used to initialize the following iteration. In this manner, the multiple shooting algorithm solves the optimal control problem and generates reachable sets which move away from the intial orbit and towards the desired target.

With each reachable set we move the controlled trajectory closer to the target stable manifold. Figure 13c shows that after eight iterations the resulting trajectory intersects the stable manifold. Combining these trajectories results in the powered portion of the transfer from the geostationary orbit to the stable manifold. Figures 13a and 13b shows the resulting trajectory, with the final trajectory shown in red which ensures the intersection with the stable invariant manifold. Once at the stable manifold, no further control input is required and the vehicle will coast towards the target periodic orbit. Figure 13d shows the control input during the powered portion of the transfer. The spacecraft maintains a bounded control magnitude during the transfer to the stable manifold.

This approach demonstrates the ability to link several computations of the reachability set to enable a more general transfer. We use eight iterations in order to transfer from the geostationary orbit to the stable manifold. This approach allows for a larger class of potential transfers which leverage the capabilities of low-thrust propulsion systems. We are able to achieve a transfer that is not possible via the standard invariant manifold approach. In addition, this example illustrates a straightforward method to depart from the natural dynamics and transfer to a large region of the phase space that is not accessible via invariant manifolds alone.

(a) Completed transfer trajectory

(b) Detailed view of transfer
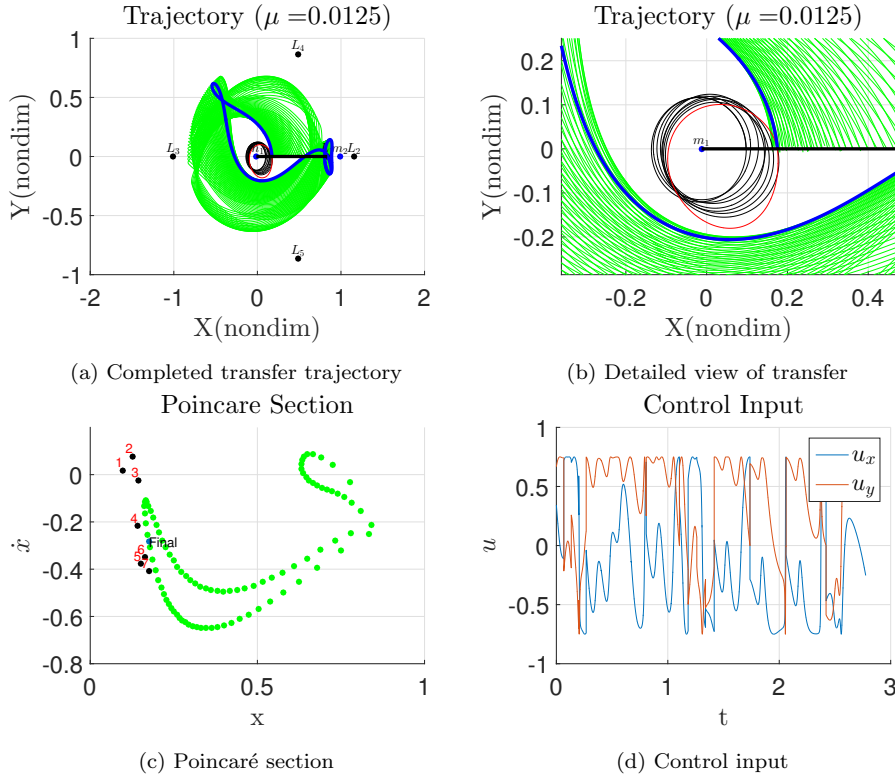
(c) Poincaré section

(d) Control input

Fig. 13: Transfer from geostationary orbit to the L_1 stable manifold using multiple iterations of the reachability set

7 Conclusions

In this paper, an optimal transfer process which combines concepts of reachability and Poincaré section is used to generate transfer between planar periodic orbits in the three-body problem. The Poincaré section allows for trajectory design on a lower dimensional phase space and simplifies the process. The indirect optimal control formulation enables straightforward method of incorporating additional path and control constraints. However, the use of optimal control techniques leads to open loop trajectories that are not robust to model uncertainties or disturbances. Lyapunov control theory, which has previously been applied to the two-body problem, is being investigated in the hope of designing closed loop control schemes for this three-body scenario [3]. This analysis has also assumed perfect attitude control and the ability to orient thrust in any direction. The addition of attitude dynamics and realistic pointing constraints would significantly improve the applicability.

Appendix A: Costate Equations of Motion

The development of the costate equations of motions begins with determining the second order partial derivatives of the gravitational potential. Due to the symmetry of partial derivatives only three terms are required and are given by

$$U_{xx_k} = (1-\mu) \left[\frac{1}{r_{1_k}^3} - \frac{3(x_k + \mu)^2}{r_{1_k}^5} \right] + \mu \left[\frac{1}{r_{2_k}^3} - \frac{3(x_k - 1 + \mu)^2}{r_{2_k}^5} \right], \tag{33}$$

$$U_{yy_k} = (1-\mu) \left[\frac{1}{r_{1_k}^3} - \frac{3y_k^2}{r_{1_k}^5} \right] + \mu \left[\frac{1}{r_{2_k}^3} - \frac{3y_k^2}{r_{2_k}^5} \right], \tag{34}$$

$$U_{xy_k} = U_{yx_k} = \frac{-3(1-\mu)(x_k + \mu)y_k}{r_{1_k}^3} - \frac{3\mu y_k (x_k - 1 + \mu)}{r_{2_k}^5}. \tag{35}$$

The gradient of Eq. (23a) is given as

$$f_{1_x} = \frac{1}{1+h^2} \left[h^2 + 1 + \frac{h^2}{2} - \frac{h^3}{2} U_{yx_k} - \frac{h^2}{2} U_{xx_k} \right], \tag{36a}$$

$$f_{1_y} = \frac{1}{1+h^2} \left[\frac{h^3}{2} - \frac{h^3}{2} U_{yy_k} - \frac{h^2}{2} U_{xy_k} \right], \tag{36b}$$

$$f_{1_{\dot{x}}} = \frac{h}{1+h^2}, \tag{36c}$$

$$f_{1_{\dot{y}}} = \frac{h^2}{1+h^2}. \tag{36d}$$

The gradient of Eq. (23b) is given as

$$f_{2_x} = h - h f_{1_x} - \frac{h^2}{2} U_{yx_k}, \tag{37a}$$

$$f_{2_y} = -h f_{1_y} + 1 + \frac{h^2}{2} - \frac{h^2}{2} U_{yy_k}, \tag{37b}$$

$$f_{2_{\dot{x}}} = -h f_{1_{\dot{x}}}, \tag{37c}$$

$$f_{2_{\dot{y}}} = h - h f_{1_{\dot{y}}}. \tag{37d}$$

The gradients of Eqs. (25c) and (25d) are given as

$$\frac{\partial r_{1_{k+1}}}{\partial \bar{x}} = \left((x_{k+1} + \mu)^2 + y_{k+1}^2 \right)^{-\frac{1}{2}} \left[(x_{k+1} + \mu) f_{1_{\bar{x}}} + y_{k+1} f_{2_{\bar{x}}} \right], \tag{38a}$$

$$\frac{\partial r_{2_{k+1}}}{\partial \bar{x}} = \left((x_{k+1} - 1 + \mu)^2 + y_{k+1}^2 \right)^{-\frac{1}{2}} \left[(x_{k+1} - 1 + \mu) f_{1_{\bar{x}}} + y_{k+1} f_{2_{\bar{x}}} \right]. \tag{38b}$$

The second order partial derivatives of the gravitational potential at $k + 1$ are given as

$$\frac{\partial U_{xx_{k+1}}}{\partial \bar{x}} = (1-\mu) \left[\frac{1}{r_{1_{k+1}}^3} f_{1_{\bar{x}}} - \frac{3(x_{k+1} + mu)}{r_{1_{k+1}}^4} \frac{\partial r_{1_{k+1}}}{\partial \bar{x}} \right] + \mu \left[\frac{1}{r_{2_{k+1}}^3} f_{1_{\bar{x}}} - \frac{-3(x_{k+1} - 1 + \mu)}{r_{2_{k+1}}^4} \frac{\partial r_{2_{k+1}}}{\partial \bar{x}} \right],$$
$$\tag{39a}$$

$$\frac{\partial U_{yx_{k+1}}}{\partial \bar{x}} = (1-\mu) \left[\frac{1}{r_{1_{k+1}}^3} f_{2_{\bar{x}}} - \frac{3y_{k+1}}{r_{1_{k+1}}^4} \frac{\partial r_{1_{k+1}}}{\partial \bar{x}} \right] + \mu \left[\frac{1}{r_{2_{k+1}}^3} f_{2_{\bar{x}}} - \frac{-3y_{k+1}}{r_{2_{k+1}}^4} \frac{\partial r_{2_{k+1}}}{\partial \bar{x}} \right].$$
$$\tag{39b}$$

The gradient of Eqs. (23c) and (23d) are given as

$$f_{3_x} = 2f_{2_x} + \frac{h}{2}\left(f_{1_x} + 1\right) - \frac{h}{2}U_{xx_{k+1}} - \frac{h}{2}U_{xx_k} \, , \tag{40a}$$

$$f_{3_y} = -2 + 2f_{2_y} + \frac{h}{2}f_{1_y} - \frac{h}{2}U_{xy_{k+1}} - \frac{h}{2}U_{xy_k} \, , \tag{40b}$$

$$f_{3_{\dot{x}}} = 1 + 2f_{2_{\dot{x}}} + \frac{h}{2}f_{1_{\dot{x}}} - \frac{h}{2}U_{x\dot{x}_{k+1}} \, , \tag{40c}$$

$$f_{3_{\dot{y}}} = 2f_{2_{\dot{y}}} \, , \tag{40d}$$

$$f_{4_x} = 2 - 2f_{1_x} + \frac{h}{2}f_{2_x} - \frac{h}{2}U_{yx_{k+1}} - \frac{h}{2}U_{yx_k} \, , \tag{41a}$$

$$f_{4_y} = -2f_{1_y} - \frac{h}{2}\left(f_{2_y} + 1\right) - \frac{h}{2}U_{yy_{k+1}} - \frac{h}{2}U_{yy_k} \, , \tag{41b}$$

$$f_{4_{\dot{x}}} = -2f_{1_{\dot{x}}} + \frac{h}{2}f_{2_{\dot{x}}} - \frac{h}{2}U_{y\dot{x}_{k+1}} \, , \tag{41c}$$

$$f_{4_{\dot{y}}} = 1 - 2f_{1_{\dot{y}}} + \frac{h}{2}f_{2_{\dot{y}}} - \frac{h}{2}U_{y\dot{y}_{k+1}} \, . \tag{41d}$$

These gradient equations are in a cascade type structure. Equations (40) and (41) are functions of Eqs. (23c) and (23d). As a result, the accuracy of the Jacobian will tend to decrease as the first order approximation errors accumulate.

Appendix B: Gauss Jordan Elimination

The costate equations of motion are given by Eq. (31) and repeated here as

$$\begin{bmatrix} f_{1_x} & f_{2_x} & f_{3_x} & f_{4_x} \\ f_{1_y} & f_{2_y} & f_{3_y} & f_{4_y} \\ f_{1_{\dot{x}}} & f_{2_{\dot{x}}} & f_{3_{\dot{x}}} & f_{4_{\dot{x}}} \\ f_{1_{\dot{y}}} & f_{2_{\dot{y}}} & f_{3_{\dot{y}}} & f_{4_{\dot{y}}} \end{bmatrix} \begin{bmatrix} \lambda_{x_{k+1}} \\ \lambda_{y_{k+1}} \\ \lambda_{\dot{x}_{k+1}} \\ \lambda_{\dot{y}_{k+1}} \end{bmatrix} = \begin{bmatrix} \lambda_{x_k} \\ \lambda_{y_k} \\ \lambda_{\dot{x}_k} \\ \lambda_{\dot{x}_k} \end{bmatrix} \, . \tag{42}$$

To determine the discrete update map $\lambda_k \rightarrow \lambda_{k+1}$ the inverse of the Jacobian matrix is required. In order to avoid the need of an explicit inversion a Gauss Jordan method is implemented. To begin, several terms are defined which are required to carry out the row operations and are defined as

$$a = -\frac{f_{1_y}}{f_{1_x}} \, , \tag{43a}$$

$$b = -\frac{f_{1_{\dot{x}}}}{f_{1_x}} \, , \tag{43b}$$

$$c = -\frac{f_{1_{\dot{y}}}}{f_{1_x}} \, , \tag{43c}$$

$$e = -\frac{f_{2_{\dot{x}}} + bf_{2_x}}{f_{2_y} + af_{2_x}} \, , \tag{43d}$$

$$f = -\frac{f_{2_{\dot{y}}} + cf_{2_x}}{f_{2_y} + af_{2_x}} \, , \tag{43e}$$

$$g = -\frac{f_{3_{\dot{y}}} + cf_{3_x} + f\left(f_{3_y} + af_{3_x}\right)}{f_{3_{\dot{x}}} + bf_{3_x} + e\left(f_{3_y} + af_{3_x}\right)} \, . \tag{43f}$$

Equation (42) is transformed to row echelon form using elementary row operations and is defined as

$$
\begin{bmatrix} \alpha_{11} & \alpha_{12} & \alpha_{13} & \alpha_{14} \\ 0 & \alpha_{22} & \alpha_{23} & \alpha_{24} \\ 0 & 0 & \alpha_{33} & \alpha_{34} \\ 0 & 0 & 0 & \alpha_{44} \end{bmatrix} \begin{bmatrix} \lambda_{x_{k+1}} \\ \lambda_{y_{k+1}} \\ \lambda_{\dot{x}_{k+1}} \\ \lambda_{\dot{y}_{k+1}} \end{bmatrix} = \begin{bmatrix} \beta_1 \\ \beta_2 \\ \beta_3 \\ \beta_4 \end{bmatrix} , \tag{44}
$$

where the terms α_{ij} and β_i are defined as follows

$$
\alpha_{11} = f_{1_x} , \tag{45a}
$$
$$
\alpha_{12} = f_{2_x} , \tag{45b}
$$
$$
\alpha_{13} = f_{3_x} , \tag{45c}
$$
$$
\alpha_{14} = f_{4_x} , \tag{45d}
$$
$$
\alpha_{22} = f_{2_y} + a f_{2_x} , \tag{45e}
$$
$$
\alpha_{23} = f_{3_y} + a f_{3_x} , \tag{45f}
$$
$$
\alpha_{24} = f_{4_y} + a f_{4_x} , \tag{45g}
$$
$$
\alpha_{33} = f_{3_{\dot{x}}} + b f_{3_x} + e \left(f_{3_y} + a f_{3_x} \right) , \tag{45h}
$$
$$
\alpha_{34} = f_{4_{\dot{x}}} + b f_{4_x} + e \left(f_{4_y} + a f_{4_x} \right) , \tag{45i}
$$
$$
\alpha_{44} = f_{4_{\dot{y}}} + c f_{4_x} + f \left(f_{4_y} + a f_{4_x} \right) + g \left(f_{4_{\dot{x}}} + b f_{4_x} + e \left(f_{4_y} + a f_{4_x} \right) \right) , \tag{45j}
$$
$$
\beta_1 = \lambda_{x_k} , \tag{45k}
$$
$$
\beta_2 = \lambda_{y_k} + a \lambda_{x_k} , \tag{45l}
$$
$$
\beta_3 = \lambda_{\dot{x}_k} + b \lambda_{x_k} + e \left(\lambda_{y_k} + a \lambda_{x_k} \right) , \tag{45m}
$$
$$
\beta_4 = \lambda_{\dot{x}_k} + c \lambda_{x_k} + f \left(\lambda_{y_k} + a \lambda_{x_k} \right) + g \left(\lambda_{\dot{x}_k} + b \lambda_{x_k} + e \left(\lambda_{y_k} + a \lambda_{x_k} \right) \right) . \tag{45n}
$$

Finally, backsubstituion is used to determine explicit equations for the discrete update map $\boldsymbol{\lambda}_k \rightarrow \boldsymbol{\lambda}_{k+1}$ which is defined as

$$
\lambda_{\dot{y}_{k+1}} = \frac{\beta_4}{\alpha_{44}} , \tag{46a}
$$

$$
\lambda_{\dot{x}_{k+1}} = \frac{\beta_3}{\alpha_{33}} - \frac{\alpha_{34}}{\alpha_{33}} \lambda_{\dot{y}_{k+1}} , \tag{46b}
$$

$$
\lambda_{y_{k+1}} = \frac{\beta_2}{\alpha_2 2} - \frac{\alpha_{33}}{\alpha_{22}} \lambda_{\dot{x}_{k+1}} - \frac{\alpha_{24}}{\alpha_{22}} \lambda_{\dot{y}_{k+1}} , \tag{46c}
$$

$$
\lambda_{x_{k+1}} = \frac{\beta_1}{\alpha_{11}} - \frac{\alpha_{12}}{\alpha_{11}} \lambda_{y_{k+1}} - \frac{\alpha_{13}}{\alpha_{11}} \lambda_{\dot{x}_{k+1}} - \frac{\alpha_{14}}{\alpha_{11}} \lambda_{\dot{y}_{k+1}} . \tag{46d}
$$

References

1. Bryson, A.E., Ho, Y.C.: Applied Optimal Control: Optimization, Estimation and Control. CRC Press (1975)
2. Campagnola, S., Skerritt, P., Russell, R.: Flybys in the planar, circular, restricted, three-body problem **113**(3), 343–368 (2012). DOI 10.1007/s10569-012-9427-x. URL http://dx.doi.org/10.1007/s10569-012-9427-x
3. Chang, D.E., Chichka, D.F., Marsden, J.E.: Lyapunov-based transfer between elliptic keplerian orbits. Discrete and Continuous Dynamical Systems Series B **2**(1), 57–68 (2002)
4. Conley, C.C.: Low energy transit orbits in the restricted three-body problem. SIAM Journal on Applied Mathematics **16**(4), pp. 732–746 (1968). URL http://www.jstor.org/stable/2099124
5. Gómez, G., Koon, W., Lo, M.W., Marsden, J., Masdemont, J., Ross, S.: Invariant manifolds, the spatial three-body problem and space mission design. In: AAS/AIAA Astrodynamics Specialist Conference, Quebec City, Canada, 2001. American Astronautical Society (2001)

6. Grebow, D.J., Ozimek, M.T., Howell, K.C.: Design of optimal low-thrust lunar pole-sitter missions. The Journal of the Astronautical Sciences **58**(1), 55–79 (2011). DOI 10.1007/BF03321159. URL `http://dx.doi.org/10.1007/BF03321159`
7. Greenwood, D.T.: Principles of Dynamics. Prentice-Hall Upper Saddle River, NJ (1988)
8. Hairer, E., Lubich, C., Wanner, G.: Geometric Numerical Integration, *Springer Series in Computational Mathematics*, vol. 31. Springer Berlin Heidelberg (2006)
9. Haque, S.E., Keidar, M., Lee, T.: Low-thrust orbital maneuver analysis for cubesat space-craft with a micro-cathode arc thruster subsystem. In: Proceedings of the thirty-third international electric propulsion conference, Electric Rocket Propulsion Society, Washington DC, USA (2013)
10. Holzinger, M., Scheeres, D.: Reachability analysis applied to space situational awareness. In: Advanced Maui Optical and Space Surveillance Technologies Conference (2009)
11. Kirk, D.E.: Optimal control theory: an introduction. Courier Corporation (2012)
12. Komendera, E.E., Scheeres, D.J., Bradley, E.: Intelligent computation of reachability sets for space missions. In: IAAI (2012)
13. Koon, W.S., Lo, M.W., Marsden, J., Ross, S.: The genesis trajectory and heteroclinic cycles. Astrodynamics 1999 **103**(Part III), 2327–2343 (1999)
14. Koon, W.S., Lo, M.W., Marsden, J.E., Ross, S.D.: Heteroclinic connections between periodic orbits and resonance transitions in celestial mechanics. Chaos: An Interdisciplinary Journal of Nonlinear Science **10**(2), 427–469 (2000)
15. Koon, W.S., Lo, M.W., Marsden, J.E., Ross, S.D.: Dynamical Systems, the Three-Body Problem and Space Mission Design. Marsden Books (2011). URL `http://www2.esm.vt.edu/~sdross/books/`
16. Lanczos, C.: The Variational Principles of Mechanics, vol. 4. Courier Corporation (1970)
17. Llibre, J., Martínez, R., Simó, C.: Tranversality of the invariant manifolds associated to the lyapunov family of periodic orbits near {L2} in the restricted three-body prob-lem. Journal of Differential Equations **58**(1), 104 – 156 (1985). DOI http://dx.doi.org/10.1016/0022-0396(85)90024-5. URL `http://www.sciencedirect.com/science/article/pii/0022039685900245`
18. Lo, M.: Libration point trajectory design **14**(1-3), 153–164 (1997). DOI 10.1023/A:1019108929089. URL `http://dx.doi.org/10.1023/A%3A1019108929089`
19. Lygeros, J.: On the relation of reachability to minimum cost optimal control. In: Decision and Control, 2002, Proceedings of the 41st IEEE Conference on, vol. 2, pp. 1910–1915 vol.2 (2002). DOI 10.1109/CDC.2002.1184805
20. Lygeros, J.: On Reachability and Minimum Cost Optimal Control. Automatica **40**(6), 917–927 (2004). DOI http://dx.doi.org/10.1016/j.automatica.2004.01.012. URL `http://www.sciencedirect.com/science/article/pii/S0005109804000263`
21. Marsden, J.E., West, M.: Discrete mechanics and variational integrators. Acta Numerica 2001 **10**, 357–514 (2001)
22. Mingotti, G., Topputo, F., Bernelli-Zazzera, F.: Low-energy, low-thrust transfers to the moon. Celestial Mechanics and Dynamical Astronomy **105**(1-3), 61–74 (2009)
23. Mingotti, G., Topputo, F., Bernelli-Zazzera, F.: Earth–mars transfers with ballistic es-cape and low-thrust capture. Celestial Mechanics and Dynamical Astronomy **110**(2), 169–188 (2011). DOI 10.1007/s10569-011-9343-5. URL `http://dx.doi.org/10.1007/s10569-011-9343-5`
24. Ozimek, M.T., Howell, K.C.: Low-thrust transfers in the earth-moon system, including applications to libration point orbits. Journal of Guidance, Control, and Dynamics **33**(2), 533–549 (2010). DOI 10.2514/1.43179. URL `http://dx.doi.org/10.2514/1.43179`
25. Ross, S.D.: The interplanetary transport network. American scientist **94**(3), 230 (2006)
26. Stoer, J., Bulirsch, R.: Introduction to Numerical Analysis, *Texts in Applied Mathematics*, vol. 12. Springer-Verlag New York (2013)
27. Szebehely, V.: Theory of orbits. the restricted problem of three bodies. New York: Academic Press **1** (1967)
28. Tanaka, K., Kawaguchi, J.: Low-thrust transfer between jovian moons using manifolds. Spaceflight Mechanics **140**(Part 3), 1935–1942 (2011). URL `http://proxygw.wrlc.org/login?url=http://search.proquest.com/docview/1022843991?accountid=11243`
29. Varaiya, P.: Reach Set Computation Using Optimal Control. In: Verification of Digital and Hybrid Systems, pp. 323–331. Springer (2000)
30. Zanzottera, A., Mingotti, G., Castelli, R., Dellnitz, M.: Intersecting invariant manifolds in spatial restricted three-body problems: Design and optimization of earth-to-halo transfers in the sun–earth–moon scenario. Communications in Nonlinear Science and Numerical Simulation **17**(2), 832–843 (2012). DOI http://dx.doi.org/10.1016/j.cnsns.2011.06.032. URL `http://www.sciencedirect.com/science/article/pii/S1007570411003479`